Rh nanoroses for isopropanol oxidation reaction

Shihui Xing[a], Zhao Liu[c], Qi Xue[a], Shiwei Yin[b], Fumin Li[b], Weiwei Cai[c,*], Shuni Li[b], Pei Chen[a], Pujun Jin[a], Hongchang Yao[d], Yu Chen[a,*]

[a] Key Laboratory of Macromolecular Science of Shaanxi Province, Key Laboratory of Applied Surface and Colloid Chemistry (Ministry of Education), Shaanxi Key Laboratory for Advanced Energy Devices, School of Materials Science and Engineering, Shaanxi Normal University, Xi'an, 710062, China
[b] School of Chemistry and Chemical Engineering, Shaanxi Normal University, Xi'an, 710062, China
[c] Sustainable Energy Laboratory, Faculty of Materials Science and Chemistry, China University of Geoscinces, Wuhan, 430074, China
[d] College of Chemistry and Molecular Engineering, Zhengzhou University, Zhengzhou, 450001, China

ABSTRACT

Reducing the overpotential of alcohol oxidation reactions is highly desirable for alkaline direct alcohol fuel cells, but there is still no substantial progress. In this study, unique three-dimensional free-standing Rh nanoroses are synthesized and applied to the isopropanol oxidation reaction. Compared to traditional Pt black electrocatalyst, as-prepared Rh nanoroses exhibit a significant negative shift both in the onset oxidation potential (Δ = 0.223 V) and peak potential (Δ = 0.435 V) as well as 7.5-fold mass activity at 0.3 V for the isopropanol oxidation reaction (IOR) in alkaline electrolyte. The density functional theory calculation indicates the enhanced IOR activity originates form the higher adsorption energy of isopropanol on Rh surface than Pt surface. Since Rh nanoroses have unparalleled activity, this research may bring a new broad of perspective on the isopropanol oxidation reaction.

1. Introduction

Direct alcohol fuel cells (DAFCs) can convert the chemical energy of liquid fuels (e.g. methanol, formic acid, ethanol, isopropanol and glycerol, etc.) into the electrical energy by electrochemical reactions [1–6]. Besides high energy conversion efficiency, no noise, and low harmful gas emissions, DAFCs also have a compact structure, room temperature start-up, and multifarious transportable fuels with high volumetric energy density [7–10]. Therefore, DAFCs are considered to be a promising and sustainable energy conversion technology. The traditional DAFCs are operated under acidic conditions, while this work mode is not perfect. Acidic operating conditions lead to slow electrode-kinetics and require corrosion-resistant electrocatalysts, so expensive platinum (Pt)-based materials with superior electrocatalytic activity are required by both the cathode and anode [11–14]. The ensuing problem is CO poisoning of Pt and fuel crossover, which reduces the activity and durability of Pt-based electrocatalysts [15,16]. To address these problems, alkaline direct alcohol fuel cells (ADAFCs) emerged as the times require [17–21].

Under alkaline operating conditions, the kinetics of both alcohol oxidation reactions (AOR) and oxygen reduction reaction (ORR) can be enhanced [22–24]. Especially at the cathode, inexpensive non-precious metal electrocatalysts also exhibit high catalytic activity for the ORR and are inert to AOR, avoiding the crossover effect [25–30]. Thus, ADAFCs attracts extensive concerns and research interests. Currently, the efficiency of ADAFCs is significantly lower than the theoretical efficiency of 100% due to the high overpotential of the ORR and AOR, hindering the commercialization process [31,32].

Compared to the cathodic ORR, optimizing anodic AOR may have more possibilities for performance enhancement of DAFCs, which not only can improve the open circuit voltage of DAFCs by selecting appropriate alcohol fuel but also elevate the stability of DAFCs by restraining the generation of CO-like intermediates [33,34]. Specifically, the different alcohol fuel molecules have different standard oxidation potential, which results in the different theoretical open circuit voltage of DAFCs. Meanwhile, the CO-like intermediates are generated during methanol/ethanol oxidation process and adsorb on the surface of traditional Pt-based electrocatalysts, which causes catalyst poisoning and prevents further reaction [35–39]. Only at high anode potentials, the Pt surface can generate reactive hydroxyl species (OH_{ad}) and eliminate CO-like intermediates to restore active sites. Fortunately, although most AOR are plagued by this poisoning process, exceptions have been discovered. The isopropanol oxidation reaction (IOR) does not produce CO-like intermediates [40,41], and thus active Pt will not be poisoned

and exhibit low oxidation overpotential, triggering research on alkaline direct isopropanol fuel cells (ADIFCs) [42,43]. Nevertheless, the oxidation potential of the IOR on Pt-based electrocatalysts is still much higher than the standard potential. In parallel, the mass activity of the IOR is lower than that of other AOR on Pt-based electrocatalysts [44]. Therefore, developing a more efficient electrocatalyst for AOR is a significant issue.

Among various AOR electrocatalysts, the electrocatalytic activity of Rh-based nanomaterials has recently been shown to be comparable to Pt-based catalysts for certain AOR [45–51]. For the IOR, Rh-based material has also been used as electrocatalysts. For example, Fujiwara et al. briefly studied the electrocatalytic performance of the Rh electrode for the IOR in acidic media [52]. Yamazaki et al. synthesized a Rh porphyrin on carbon black, which exhibited good electrocatalytic activity with low overpotential for the IOR in alkaline electrolyte [53]. However, the activity of metal Rh nanocatalysts for the IOR remains to be studied. On the one hand, the morphology control synthesis of Rh nanostructures is difficult due to the high surface energy. On the other hand, the research of Rh-based electrocatalysts is still in a rising period compared to conventional Pt-based and Pd-based materials. Therefore, studying the IOR performance of Rh nanostructures is of great significance for the development of Rh-based electrocatalysts and the practical application of ADIFCs. So herein, we developed rose-like Rh nanostructures and investigated their electrocatalytic performance for the IOR in alkaline solution. Surprisingly, compared with commercial Pt black, Rh nanoroses synchronously achieve lower oxidation peak potential (435 mV peak potential shift) and higher mass activity (7.4-fold mass activity enhancement) for the IOR. This exciting result will intensively improve the efficiency of ADIFCs and drive the commercialization process.

2. Experimental section

2.1. Reagents and chemicals

Rhodium (III) chloride hydrate (RhCl$_3$·3H$_2$O) was purchased from Aladdin Industrial Co. (Shanghai, China). Isopropanol (CH$_3$CHOHCH$_3$, 99.7%), potassium hydroxide (KOH, > 85%), formaldehyde aqueous solution (HCHO, 37.0–40.0%) and pyridine (99.5%) were supplied from Sinopharm Chemical Reagent Co., Ltd. Nafion solution (5 wt%) was supplied from Sigma Aldrich. Commercial Pt black was supplied from Johnson Matthey Corporation.

2.2. Preparation of Rh nanoroses

Rh nanoroses were synthesized by a hydrothermal process. Aqueous solutions of RhCl$_3$·3H$_2$O (0.075 M, 2.0 mL), pyridine (80 μL), HCHO (2.0 mL) were added into ultrapure water (24 mL). Then the mixture solution was heated at 160 °C for 5 h in a high-pressure vessel. Finally, the products were washed by ultrapure water for four times and dried at 30 °C in a vacuum oven.

2.3. Characterizations

The morphology, crystalline structure, surface information and composition were conducted by scanning electron microscope (SEM, SU-8020), Transmission electron microscope (TEM, JEM-2100 F), X-ray diffraction (XRD, DX-2700) and X-ray photoelectron spectroscopy (XPS, Thermo VG Scientific ESCALAB 250). Ultraviolet-visible spectroscopy (UV–vis) was used to test the interaction of pyridine and Rh^{3+} (UV-3600, SHIMADZU). Thickness of Rh nanosheets was measured by atomic force microscope (AFM, Dimension ICON, Brucker).

2.4. Electrochemical measurements

Cyclic voltammetry (CV) tests were performed on CHI 660 D electrochemical analyzer. The electrocatalysts (2 mg) was dispersed in a mixed solution of ethanol and deionized water (1.0 mL, ethanol : deionized water = 3:1). Then, the electrocatalysts ink (4 μL) was deposited on a glassy carbon electrode (diameter: 3 mm) and covered with Nafion (10 μL, 0.05 wt%). And the electrocatalyst modified glassy carbon electrode was used as working electrode. A graphite electrode was used as auxiliary electrode. And a saturated calomel electrode (SCE) was used as reference electrode. All potentials in this work were converted to the reversible hydrogen electrode (RHE), using the following equation ($E_{RHE} = E_{SCE} + 0.059 \, pH + 0.2412$).

2.5. Fuel cell tests

The catalyst ink was prepared using the following weight ratio: catalyst/isopropanol/deionized water/5 wt% Nafion of 1/12/12/11. The ink was ultrasonicated for 1 h and then sprayed onto one side of a carbon paper (TGP-H-060, Troay) with an effective area of ca. 5 cm^2 until the loading reached 4 mg cm^{-2}. Rh nanoroses (or Pt black) were used as anode catalyst while homemade NiCo$_2$O$_4$ was used as cathode catalyst layer. The anode electrode, porous membrane and cathode electrode were then assembled together with the fuel reservoir and current collectors by screws at a certain pressure to form a passive fuel cell. 5 M KOH + 1 M isopropanol solution was used as fuel and electrolyte and ambient air was used as oxidant. Polarization curves of the air-breathing fuel cells were collected by Arbin battery test system at 25 °C.

2.6. Computational method

The calculated lattice parameters for Pt bulk are a = b = 3.92 Å, and a = b = 3.80 Å for Rh bulk, respectively. The most exposed (111) crystallographic plane was selected to study the isopropanol adsorption. Then, the computational methodology and the adsorption model will be further considered.

Based on spin polarized Density Functional Theory, namely DFT, the first principles calculations were implemented through the Vienna Ab-initio Simulation Package (VASP) [54–56]. The projector-augmented wave (PAW) method was used to solve the Kohn-Sham equations with periodic boundary conditions [57,58]. The Perdew-Burke-Ernzerhof form of the spin-polarized generalized gradient approximation was employed to calculate exchange and correlation energy [59]. A 400 eV kinetic energy cutoff was employed for calculation in the plane wave basis set expansion. The gamma-centered Monkhorst-Pack scheme is 3 × 3 × 1 k-points grid, which was employed for integration over the Brillouin zone [60]. The geometry optimization tolerance was 0.02 eV/Å. The total energy difference was set to down to ~0.01 meV/atom. The van der Waals interaction was explained by the Grimme's DFT-D3 method [61].

The stabilization energy for Pt-CH$_3$CHOHCH$_3$ and Rh-CH$_3$CHOHCH$_3$ was defined with respect to isolated atoms as following:

$$E_{ad} = E_{gas@catalyst} - E_{gas} - E_{catalyst}$$

where $E_{gas@catalyst}$ is the energy of the optimized adsorption structure, E_{gas} is the energy of the isolated gas molecule, and $E_{catalyst}$ are the energy of the catalyst (Pt or Rh).

Considering accuracy and computational time, 7 layers' slab was selected and separated in the [111]-direction by a vacuum region. The 15 Å distance of 15 Å was considered to prevent periodic configurations from spurious interaction. Given that isopropanol adsorption on the Pt (111) and Rh(111) surface exhibits low coverage (1/9 ML), we optimized the molecule-surface distance to relax the first 3 metal layers until the total energy reached a 0.1 meV convergence. Meanwhile, we fixed the 4 remained metal layers. Finally, the isopropanol adsorption at the top site on the Pt(111) or Rh(111) surface was investigated.
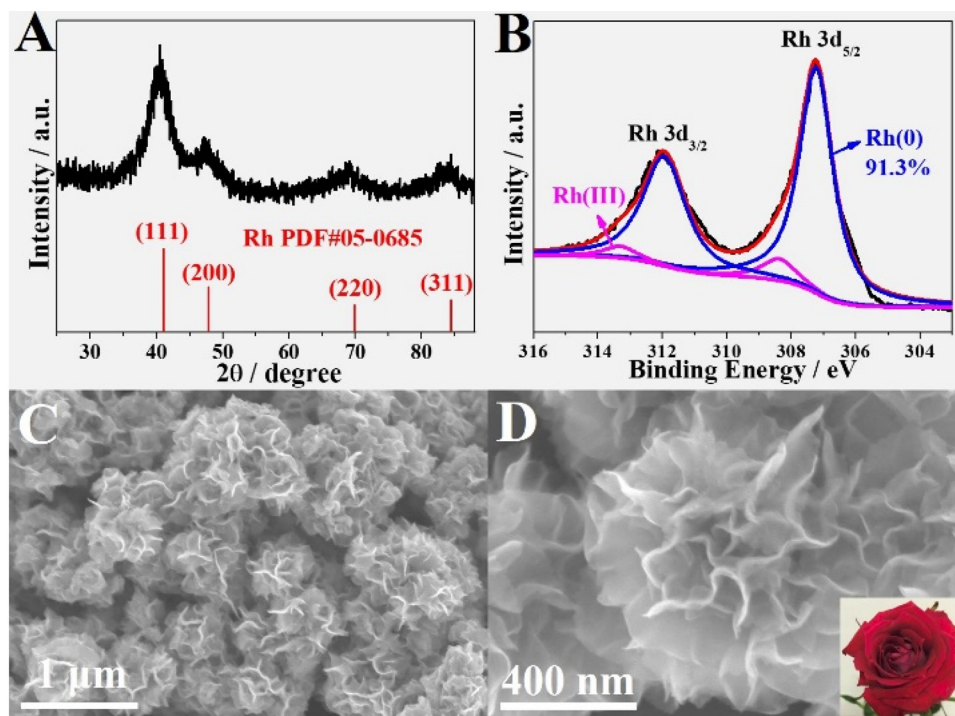
Fig. 1. (A) XRD pattern and (B) XPS Rh 3d, (C and D) SEM (inset: digital photo of rose) of Rh nanoroses.

3. Results and discussion

3.1. Synthesis and physical characterization of Rh nanoroses

Rh nanoroses were synthesized by a facile hydrothermal process at 160 °C, in which $RhCl_3$, formaldehyde, pyridine, and water were used as precursor, reducing agent, additive, and solvent, respectively. The successful preparation of Rh nanoroses was confirmed by XRD and XPS. XRD pattern of products exhibits the four distinct and broadened diffraction peaks at 41.07°, 47.78°, 69.88°, and 84.39°, respectively, which are consistent with the standard PDF diffraction data of face-centered-cubic Rh (PDF#05-0685, Fig. 1A). The surface composition and element valence of products were analyzed by XPS. The recorded XPS full spectrum show distinct Rh 3d signal (Fig. S1). The fine Rh 3d spectrum of products can be further deconvoluted into two sets of peaks corresponding to photoelectron binding energies of metal Rh and Rh oxide, respectively (Fig. 1B). As observed, the content of metal Rh is dominant (91.3%), indicating that $RhCl_3$ is successfully reduced. Additionally, the formation of Rh oxide is attributed to the slight oxidation of Rh in the air because of a high surface energy of the ultrafine nanostructures [62,63]. In general, the metal Rh is considered to be the active site. However, partial oxidation of Rh nanostructures can alter the oxophilicity of their surface, thereby affecting their electrocatalytic activity. Herein, it is hard to precisely control the oxidation degree of Rh nanostructures, and their surface properties are constantly changing during electrochemical process. Therefore, the role of oxygen on the surface of Rh nanostructures is not discussed in the subsequent catalytic process. SEM was first adopted to recognize the morphological features of products. The SEM images show that the products are three-dimensional (3D) free-standing Rh nanoroses assembled from ultrathin nanosheets, like rose (Fig. 1C and D). Such nanostructures are considered to be very suitable for electrocatalytic reactions. On the one hand, its structural characteristics can effectively inhibit Ostwald ripening, resulting in improved structural stability and catalytic durability [64,65]. On the other hand, the construction of 3D architectures also exhibits a large specific surface area (more active sites) and fast ion and mass transport, showing optimal reaction kinetics [66,67]. Actually, the

formation of these well-defined Rh nanoroses benefits from the addition of a small amount of pyridine. The control experiment shows that, without the addition of pyridine, the product obtained at the same pH shows a significant aggregation (Fig. S2). Further tracking experiments reveal that pyridine can slow down the reduction rate of Rh^{3+} to achieve the control of morphology (Fig. S3), which can be attributed to the coordination interaction of pyridine with Rh^{3+}. As confirmed by UV–vis, the absorption peak of the $RhCl_3$ aqueous solution significantly change after the addition of pyridine (Fig. S4A). Further linear sweep voltammetry reveals a significant decrease in the reduction potential of Rh^{3+} after the coordination interaction of pyridine and Rh^{3+} (Fig. S4B).

TEM was used to observe the fine structure of Rh nanoroses. TEM image of single Rh nanoroses shows distinct bright and dark regions, which stem from the image overlay and the different spatial extension directions of subunit nanosheets (Fig. 2A). Enlarged TEM and high resolution TEM (HRTEM) images of Rh nanoroses reveal more structural information. The most obvious feature is that the ultrafine grains with different orientations constitute a single Rh nanosheet (Fig. 2B–C). This fact indicates that the generation of Rh nanoroses does not follow the epitaxial growth mechanism, but the oriented attachment process with two-dimensional confined, which is related to the tendency of Rh to crystallize into sheet-like nanostructures [68,69]. Furthermore, HRTEM image indicates there are a large number of atomic-level coupled interfaces made up of kinks and intergranular atoms; most of the lattice spacing matches the interplanar spacing of the Rh(111) plane, indicating lots of exposed Rh(111) surfaces (Fig. 2C). In particular, these atoms at the defect sites are subjected to lattice distortions and strains in different directions, and in turn their intrinsic properties are quite different from those in the bulk phase, which tend to have superior catalytic activity for various catalytic/electrocatalytic reactions [70–75]. The corresponding selected area electron diffraction (SAED) image also suggests low crystallinity of individual Rh nanosheet (Fig. 2C inset). Considering the thickness of subunit nanosheets determines the utilization of Rh, the corresponding accurate measurement was performed by AFM. The results show that the thickness of the Rh nanosheets is only 2 nm, suggesting a veritable ultrathin structure
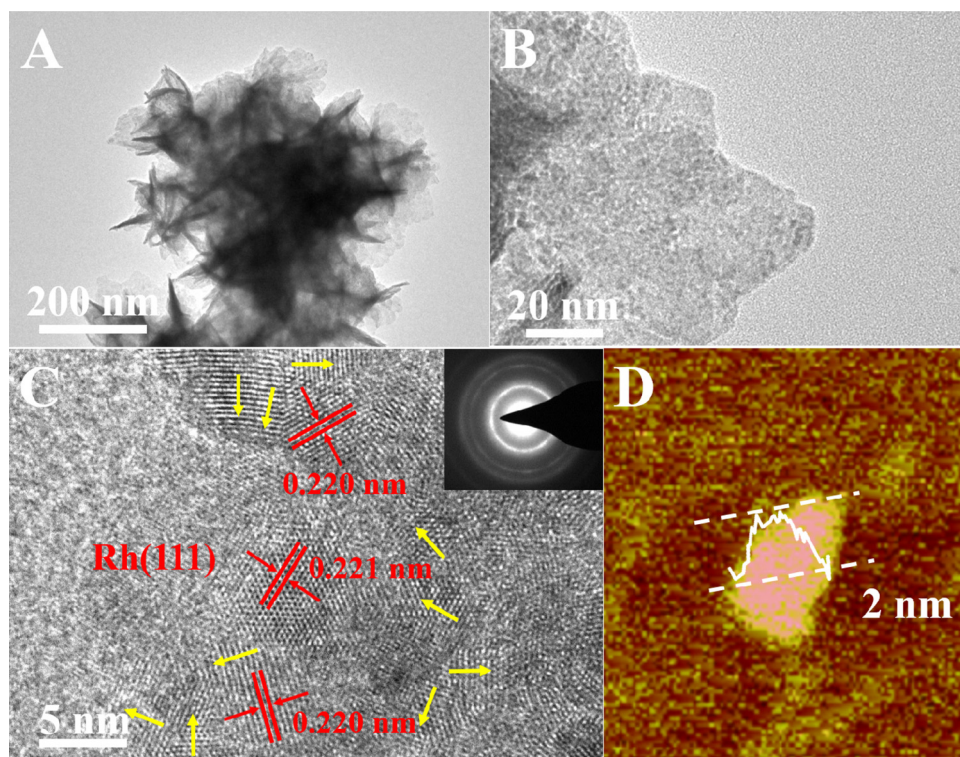
Fig. 2. (A) TEM, (B) enlarged TEM, (C) HRTEM images of Rh nanoroses (inset: corresponding SAED image; the arrow indicates the growth direction of the crystal lattice). (D) AFM image of subunit nanosheet obtained from Rh nanoroses.
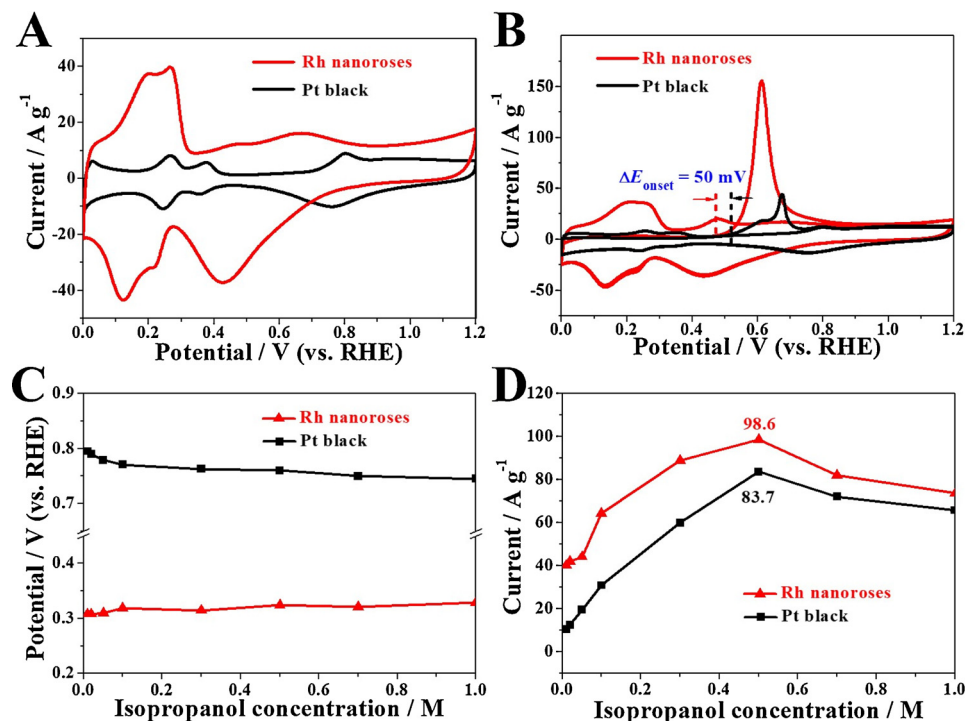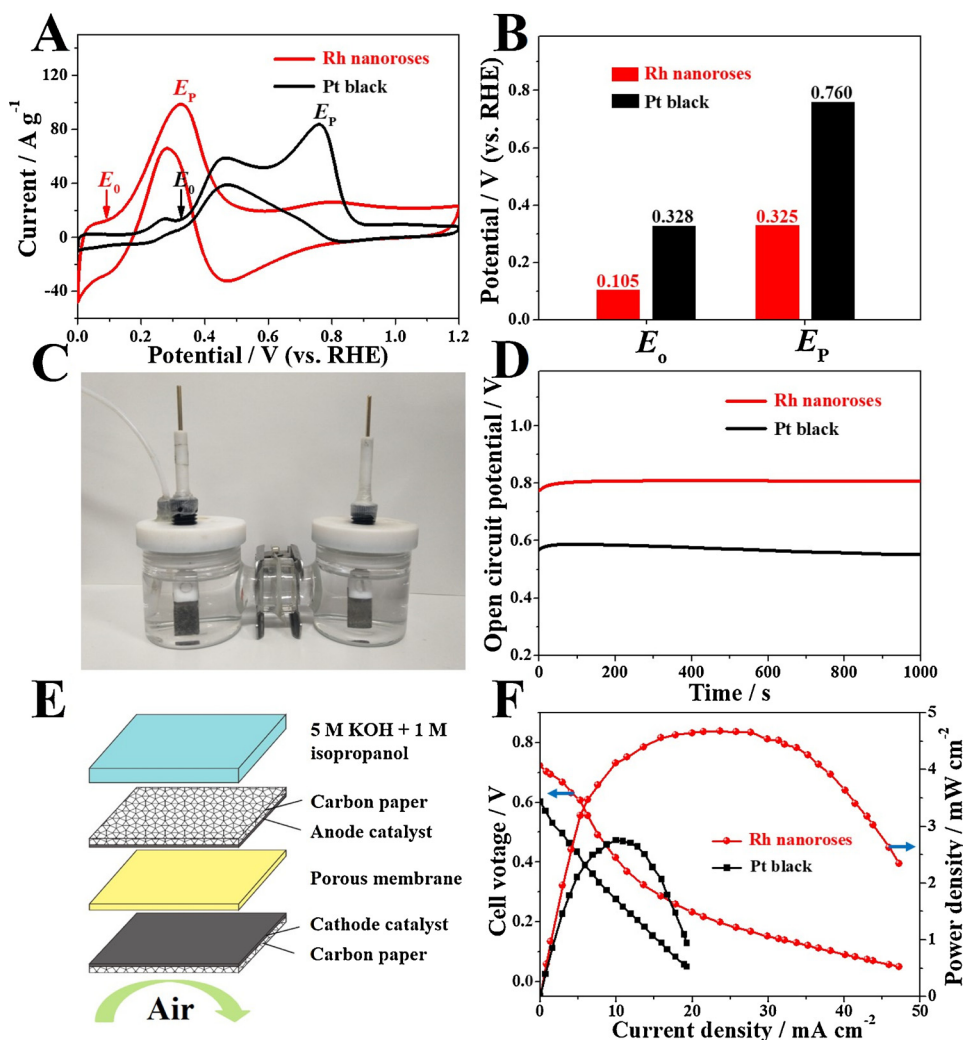

Fig. 3. (A) CV and (B) CO-stripping CV curves of Rh nanoroses and Pt black in 1 M KOH solution (scan rate: 50 mV s^{-1}). (C) Peak potential and (D) peak current of the IOR on Rh nanoroses and Pt black in 1 M KOH + 0.01–1 M isopropanol solutions (scan rate: 50 mV s^{-1}).

(Fig. 2D).

3.2. IOR activity of Rh nanoroses

Given that these physical characterizations indicate that Rh na-noroses have various advantages as electrocatalysts, their

electrochemical behavior is subsequently tested. The electrochemical performance of commercial Pt black was also analyzed as comparisons. CV was performed in 1 M KOH solution (Fig. 3A). Compared to Pt black, Rh nanoroses exhibit larger hydrogen adsorption/desorption region, suggesting larger electrochemically active surface area (ECASA). The quantitative calculation indicates that ECASA$_H$ of Rh nanoroses is

Fig. 4. (A) CV curves of Rh nanoroses and Pt black in 1 M KOH + 0.5 M isopropanol solution (scan rate: 50 mV s^{-1}). (B) Onset oxidation and peak potentials of the IOR on Rh nanoroses and Pt black. (C) Digital photo of the simple ADIFC device for measuring open circuit voltage. (D) Open circuit potential-time curves of the simple ADIFCs with different anode catalyst (the cathode catalyst is nitrogen-doped graphene aerogels [25]). (E) Configuration of porous membrane air-breathing passive direct isopropanol fuel cell. (F) Polarization and power density curves of Rh nanoroses and Pt black based air-breathing passive direct isopropanol fuel cells at 25 °C and ambient pressure.
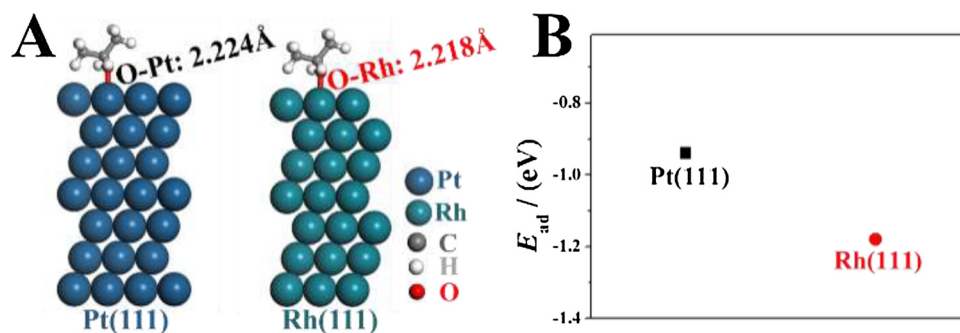

Fig. 5. (A) Schematic top view of isopropanol adsorption on Pt(111) and Rh(111) crystal plane. (B) E_{ad} of isopropanol on top sites of Pt(111) and Rh(111) crystal plane.

46.5 m^2 g^{-1}, which is much higher than that of Pt black (13.9 m^2 g^{-1}). 3D free-standing structures and ultrafine subunits are responsible for the high ECASA of Rh nanoroses. ECASA values of both electrocatalysts were also measured by CO-stripping experiment [76]. After calculating the charge integral of CO oxidation, ECASA$_{CO}$ of Rh nanoroses and Pt black were measured to be 47.0 and 13.5 m^2 g^{-1}, respectively, consistent with the above ECASA$_H$ (Fig. 3B). Strikingly, the onset stripping potential of CO on Rh nanoroses is lower than that of Pt black, indicating an enhanced activity of Rh nanoroses for CO electrooxidation.

Studying AOR in alkaline media is an important basic work for ADAFCs. Here, isopropanol is selected as a fuel molecule, which is less

volatile and toxic than conventional methanol. To understand the electrocatalytic activity of Rh nanoroses and traditional Pt black catalyst for the IOR, the effect of isopropanol concentration on electrochemical response was investigated. With the addition of isopropanol (from 0.01 M to 1 M), the electrocatalytic activities of Rh nanoroses and Pt black show some in common (Fig. S5). The peak potential does not move significantly, while the peak currents exhibit a volcano correlation (Fig. 3C and D). Coincidentally, both Rh nanoroses and Pt black exhibit the highest catalytic activity for the IOR when the isopropanol concentration is 0.5 M, suggesting a shared optimal reaction condition.

Further observations and comparisons confirm that the catalytic
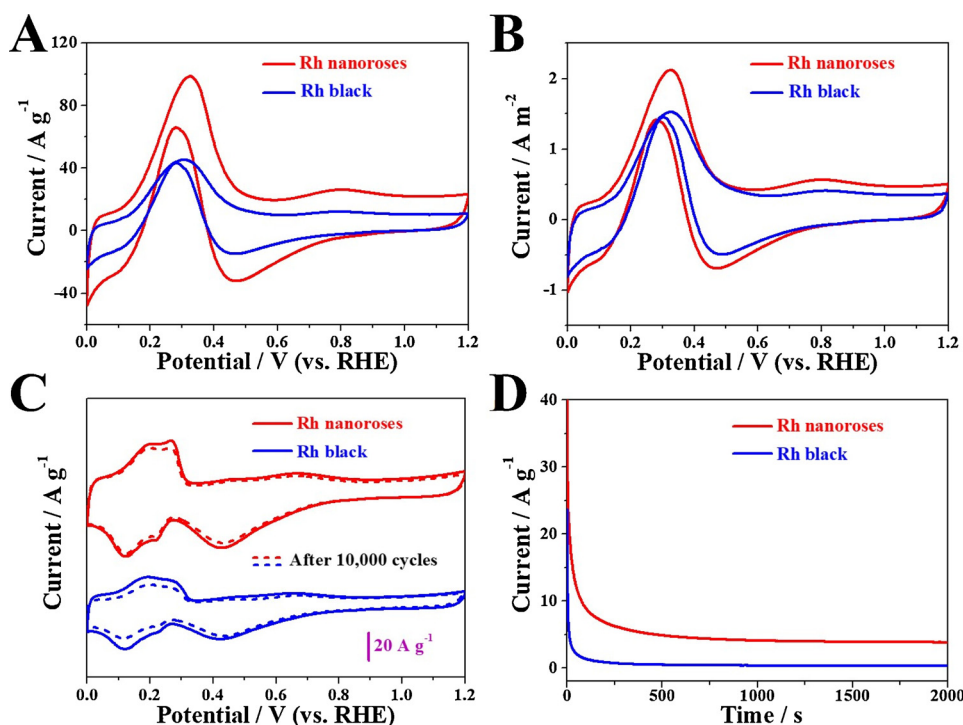
activity of Pt black for IOR is eclipsed by that of Rh nanoroses due to higher peak current (83.7 A g^{-1} vs. 98.6 A g^{-1}) and negative peak potential (E_p, 0.760 V vs. 0.325 V) of the latter (Fig. 4A and B). At 0.3 V potential, a typically anode working voltage for the DAFCs [77], the mass activity of AOR on Rh nanoroses is as high as 7.5 times that on Pt black (12.6 A g^{-1} vs. 94.7 A g^{-1}). Moreover, compared with Pt black, the onset oxidation potential (E_o) of Rh nanoroses is negatively shifted by 223 mV, which will increase the open circuit voltage and in turn improve the efficiency of ADIFCs (Fig. 4B). This remarkable performance improvement is necessarily determined by the physical and chemical properties of Rh nanomaterials. To further assess the practical feasibility of Rh nanoroses to replace commercial Pt black for ADIFCs, a simple method for measuring open circuit voltage was implemented (Fig. 4C). Under the same test conditions, Rh nanoroses provide a stable open circuit voltage of 0.810 V, which is 240 mV higher than Pt black (Fig. 4D). Since the cathode electrocatalysts are the same, the large increase in open circuit voltage is entirely attributable to the optimized anode electrocatalyst. To evaluate the performance of the Rh nanoroses in fuel cell devices, air-breathing passive ADIFCs based on porous membrane was assembled (Fig. 4E). For the ORR in alkaline media, NiCo$_2$O$_4$ catalyst was applied as cathode catalyst. By using 5 M KOH + 1 M isopropanol solution as fuel in the anode fuel reservoir, polarization curves of the passive ADIFCs can be collected (Fig. 4F). As desired, Rh nanoroses exhibited an open circuit voltage of 0.72 V, which is 0.12 V higher than that of Pt black. A peak power density reached 4.7 mW cm^{-2} at room temperature and ambient pressure, which is 70% higher than that of the Pt black catalyst with the same loading. It can be concluded that the Rh nanoroses is able to outperform Pt black in ADIFCs under the same condition, although the power density output is still insufficient due to unoptimized electrode structure, membrane, fuel concentration and cathode catalyst.

3.3. IOR activity enhancement mechanism

To shed light on the superior IOR activity of Rh nanoroses, the adsorption energy (E_{ad}) of isopropanol on Pt(111) and Rh(111) surfaces were calculated by DFT based on the above HRTEM analysis (Fig. 2C). In general, isopropanol can be adsorbed at top site, bridge site and hollow site of Pt(111) or Rh(111) crystal plane. However, the optimizational results indicate that isopropanol finally adsorbs on top sites, which is the preferred adsorption configuration with lowest system energy (Fig. 5A). Specifically, the isopropanol-Rh(111) exhibits smaller interaction distance (2.218 Å) than the isopropanol-Pt(111) (2.224 Å). Furthermore, the adsorption energy (E_{ad}) of isopropanol on top sites is calculated, and the E_{ad} values are −0.94 eV at Pt(111) and −1.18 eV at Rh(111) crystal plane, respectively (Fig. 5B). The higher adsorption energy between isopropanol and the Rh(111) crystal plane reveals a stronger interaction than the isopropanol-Pt(111), which facilitates the succedent electrocatalytic reaction [78,79]. Indeed, according to Sabatier's principle, larger binding energies tend to cause the reaction to occur at lower overpotential, which is consistent with electrochemical test results.

3.4. Activity comparison between Rh nanoroses and commercial Rh black

The above experimental and theoretical results have demonstrated the Rh nanoroses with superior electrocatalytic activity for the IOR is competent for traditional Pt as anode electrocatalysts of ADIFCs, so the electrocatalytic performance of commercial Rh black was also investigated. SEM image of Rh black indicates it is composed of stacked nanoparticles (Fig. S6). The basic CV tests indicate that the electrochemical behavior of Rh black is consistent with the Rh nanoroses except for the smaller hydrogen adsorption/desorption region (Fig. S7), revealing a low ECASA (29.7 m^2 g^{-1}). The IOR measurement curves shows that the E_p and E_o of Rh black are similar to that of Rh nanoroses, suggesting the essential activity of Rh (Fig. 6A). Compared with Rh black, Rh nanoroses still shows better mass activity and specific activity, highlighting the structural superiority of Rh nanoroses (Fig. 6A and B). In particular, the high ECASA and rich defects endow Rh nanoroses with more and better active sites for the IOR.

The electrocatalytic stabilities of Rh nanoroses and Rh black were further investigated. After 10,000 cycles of electrochemical scanning (0.4–1.2 V), the ECASA of Rh nanoroses was reduced by 8.8% below 24.3% of Rh black (Fig. 6C). The good stability of Rh nanoroses is attributed to the corrosion resistance of Rh in an alkaline environment and a special 3D free-standing structure. It is known that the structural

stability of electrocatalysts is an important foundation for catalytic stability. As expected, the chronoamperometry curves tested at 0.3 V indicate that the Rh nanoroses have better electrocatalytic stability for IOR than Rh black (Fig. 6D).

4. Conclusion

In summary, 3D free-standing Rh nanoroses assembled from ultra-thin nanosheets were synthesized by a facile wet chemical method, which had a large ECASA and rich grain boundary defects. Electrochemical tests indicated that Rh nanoroses exhibited an onset oxidation potential of 105 mV and an oxidation peak potential of 325 mV for the IOR, which was significantly lower than Pt black, achieving a significant reduction in overpotential. The mass activity (94.7 A g^{-1}) of Rh nanoroses for the IOR was far superior to that of Pt black (12.6 A g^{-1}) at 0.3 V. The open circuit voltage test showed that the Rh nanoroses as anode electrocatalysts drastically increased the voltage value by 0.24 V relative to Pt black. The DFT simulations indicated that the isopropanol had a higher adsorption energy at Rh(111) crystal plane than Pt(111) crystal plane, proving the excellent IOR activity of Rh nanoroses. Benefiting from the unique structure, the electrocatalytic activity and stability of Rh nanoroses certainly outperformed commercial Pt black and Rh black. This study provided an instructive insight into the Rh-based nanomaterials as a highly efficient electrocatalyst for the AOR.

Declaration of Competing Interest

The authors declare that they have no known competing financial interests or personal relationships that could have appeared to influence the work reported in this paper.

Acknowledgements

Appendix A. Supplementary data

Supplementary material related to this article can be found, in the online version, at doi:https://doi.org/10.1016/j.apcatb.2019.118082.

References

[1] K. Chen, L. Shi, Y. Zhang, Z. Liu, Scalable chemical-vapour-deposition growth of three-dimensional graphene materials towards energy-related applications, Chem. Soc. Rev. 47 (2018) 3018–3036.

[2] M.A.Z.G. Sial, M.A.U. Din, X. Wang, Multimetallic nanosheets: synthesis and applications in fuel cells, Chem. Soc. Rev. 47 (2018) 6175–6200.

[3] J. Mao, W. Chen, D. He, J. Wan, J. Pei, J. Dong, Y. Wang, P. An, Z. Jin, W. Xing, H. Tang, Z. Zhuang, X. Liang, Y. Huang, G. Zhou, L. Wang, D. Wang, Y. Li, Design of ultrathin Pt-Mo-Ni nanowire catalysts for ethanol electrooxidation, Sci. Adv. 3 (2017) e1603068.

[4] Q. Feng, S. Zhao, D. He, S. Tian, L. Gu, X. Wen, C. Chen, Q. Peng, D. Wang, Y. Li, Strain engineering to enhance the electrooxidation performance of atomic-layer Pt on intermetallic Pt₃Ga, J. Am. Chem. Soc. 140 (2018) 2773–2776.

[5] Y. Li, L. Liang, C. Liu, Y. Li, W. Xing, J. Sun, Self-healing proton-exchange membranes composed of nafion-oly(vinyl alcohol) complexes for durable direct methanol fuel cells, Adv. Mater. 30 (2018) 1707146.

[6] J. Lai, F. Lin, Y. Tang, P. Zhou, Y. Chao, Y. Zhang, S. Guo, Efficient bifunctional polyalcohol oxidation and oxygen reduction electrocatalysts enabled by ultrathin PtPdM (M = Ni, Fe, Co) nanosheets, Adv. Energy Mater. 9 (2019) 1800684.

[7] G.-F. Chen, Y. Luo, L.-X. Ding, H. Wang, Low-voltage electrolytic hydrogen production derived from efficient water and ethanol oxidation on fluorine-modified FeOOH anode, ACS Catal. 8 (2017) 526–530.

[8] L. Zhang, L.-X. Ding, H. Chen, D. Li, S. Wang, H. Wang, Self-supported PtAuP alloy nanotube arrays with enhanced activity and stability for methanol electro-oxidation, Small 13 (2017) 1604000.

[9] S. Xue, W. Deng, F. Yang, J. Yang, I.S. Amiinu, D. He, H. Tang, S. Mu, Hexapod PtRuCu nanocrystalline alloy for highly efficient and stable methanol oxidation, ACS Catal. 8 (2018) 7578–7584.

[10] D. He, H. Tang, Z. Kou, M. Pan, X. Sun, J. Zhang, S. Mu, Engineered graphene materials: synthesis and applications for polymer electrolyte membrane fuel cells, Adv. Mater. 29 (2017) 1601741.

[11] F.-M. Li, X.-Q. Gao, S.-N. Li, Y. Chen, J.-M. Lee, Thermal decomposition synthesis of functionalized PdPt alloy nanodendrites with high selectivity for oxygen reduction reaction, NPG Asia Mater. 7 (2015) e219.

[12] Z. Zhang, Q. Wu, K. Mao, Y. Chen, L. Du, Y. Bu, O. Zhuo, L. Yang, X. Wang, Z. Hu, Efficient ternary synergism of platinum/tin oxide/nitrogen-doped carbon leading to high-performance ethanol oxidation, ACS Catal. 8 (2018) 8477–8483.

[13] T.V. Cleve, S. Moniri, G. Belok, K.L. More, S. Linic, Nanoscale engineering of efficient oxygen reduction electrocatalysts by tailoring the local chemical environment of Pt surface sites, ACS Catal. 7 (2017) 17–24.

[14] D. Li, Y. Jia, G. Chang, J. Chen, H. Liu, J. Wang, Y. Hu, Y. Xia, D. Yang, X. Yao, A defect-driven metal-free electrocatalyst for oxygen reduction in acidic electrolyte, Chemistry 4 (2018) 2345–2356.

[15] Y. Liu, M. Wei, D. Raciti, Y. Wang, P. Hu, J.H. Park, M. Barclay, C. Wang, Electro-oxidation of ethanol using Pt₃Sn alloy nanoparticles, ACS Catal. 8 (2018) 10931–10937.

[16] H.-C. Yang, R.Z. Waldman, M.-B. Wu, J. Hou, L. Chen, S.B. Darling, Z.-K. Xu, Dopamine: just the right medicine for membranes, Adv. Funct. Mater. 28 (2018) 1705327.

[17] S. Maurya, J.H. Dumont, C.N. Villarrubia, I. Matanovic, D. Li, Y.S. Kim, S. Noh, J. Han, C. Bae, H.A. Miller, C.H. Fujimoto, D.R. Dekel, Surface adsorption affects the performance of alkaline anion-exchange membrane fuel cells, ACS Catal. 8 (2018) 9429–9439.

[18] E. Antolini, E.R. Gonzalez, Alkaline direct alcohol fuel cells, J. Power Sources 195 (2010) 3431–3450.

[19] J.R. Varcoe, P. Atanassov, D.R. Dekel, A.M. Herring, M.A. Hickner, P.A. Kohl, A.R. Kucernak, W.E. Mustain, K. Nijmeijer, K. Scott, T. Xu, L. Zhuang, Anion-exchange membranes in electrochemical energy systems, Energy Environ. Sci. 7 (2014) 3135–3191.

[20] B. Dong, W. Li, X. Huang, Z. Ali, T. Zhang, Z. Yang, Y. Hou, Fabrication of hierarchical hollow Mn doped Ni(OH)₂ nanostructures with enhanced catalytic activity towards electrochemical oxidation of methanol, Nano Energy 55 (2019) 37–41.

[21] Z. Wang, J. Du, Y. Zhang, J. Han, S. Huang, A. Hirata, M. Chen, Free-standing nanoporous gold for direct plasmon enhanced electro-oxidation of alcohol molecules, Nano Energy 56 (2019) 286–293.

[22] T. Van Cleve, E. Gibara, S. Linic, Electrochemical oxygen reduction reaction on Ag nanoparticles of different shapes, ChemCatChem 8 (2016) 256–261.

[23] Y. Hao, Y. Xu, W. Liu, X. Sun, Co/CoP embedded in a hairy nitrogen-doped carbon polyhedron as an advanced tri-functional electrocatalyst, Mater. Horiz. 5 (2018) 108–115.

[24] Q. Shi, S. Fu, C. Zhu, J. Song, D. Du, Y. Lin, Metal-organic frameworks-based catalysts for electrochemical oxygen evolution, Mater. Horiz. 6 (2019) 684–702.

[25] Q. Xue, Y. Ding, Y. Xue, F. Li, P. Chen, Y. Chen, 3D nitrogen-doped graphene aerogels as efficient electrocatalyst for the oxygen reduction reaction, Carbon 139 (2018) 137–144.

[26] N. Jia, Q. Weng, Y. Shi, X. Shi, X. Chen, P. Chen, Z. An, Y. Chen, N-doped carbon nanocages: bifunctional electrocatalysts for the oxygen reduction and evolution reactions, Nano Res. 11 (2018) 1905–1906.

[27] A. Han, W. Chen, S. Zhang, M. Zhang, Y. Han, J. Zhang, S. Ji, L. Zheng, Y. Wang, L. Gu, C. Chen, Q. Peng, D. Wang, Y. Li, A polymer encapsulation strategy to synthesize porous nitrogen-doped carbon-nanosphere-supported metal isolated-single-atomic-site catalysts, Adv. Mater. 30 (2018) 1706508.

[28] Y. Chen, S. Ji, C. Chen, Q. Peng, D. Wang, Y. Li, Single-atom catalysts: synthetic strategies and electrochemical applications, Joule 2 (2018) 1242–1264.

[29] T. Li, Y. Lv, J. Su, Y. Wang, Q. Yang, Y. Zhang, J. Zhou, L. Xu, D. Sun, Y. Tang, Anchoring CoFe₂O₄ nanoparticles on N-doped carbon nanofibers for high-performance oxygen evolution reaction, Adv. Sci. 4 (2017) 1700226.

[30] G. Fu, X. Yan, Y. Chen, L. Xu, D. Sun, J.-M. Lee, Y. Tang, Boosting bifunctional oxygen electrocatalysis with 3D graphene aerogel-supported Ni/MnO particles, Adv. Mater. 30 (2018) 1704609.

[31] N. Erini, V. Beermann, M. Gocyla, M. Gliech, M. Heggen, R.E. Dunin-Borkowski, P. Strasser, The effect of surface site ensembles on the activity and selectivity of ethanol electrooxidation by octahedral PtNiRh nanoparticles, Angew. Chem. Ed. Int. 129 (2017) 6633–6638.

[32] A.A. Gewirth, J.A. Varnell, A.M. DiAscro, Nonprecious metal catalysts for oxygen reduction in heterogeneous aqueous systems, Chem. Rev. 118 (2018) 2313–2339.

[33] N. Benipal, J. Qi, Q. Liu, W. Li, Carbon nanotube supported PdAg nanoparticles for electrocatalytic oxidation of glycerol in anion exchange membrane fuel cells, Appl. Catal. B-Environ. 210 (2017) 121–130.

[34] L. Wang, S. Zhu, N. Marinkovic, S. Kattel, M. Shao, B. Yang, J.G. Chen, Insight into the synergistic effect between nickel and tungsten carbide for catalyzing urea electrooxidation in alkaline electrolyte, Appl. Catal. B-Environ. 232 (2018) 365–370.

[35] W. Zhang, Y. Yang, B. Huang, F. Lv, K. Wang, N. Li, M. Luo, Y. Chao, Y. Li, Y. Sun, Z. Xu, Y. Qin, W. Yang, J. Zhou, Y. Du, D. Su, S. Guo, Ultrathin PtNiM (M = Rh, Os, and Ir) nanowires as efficient fuel oxidation electrocatalytic materials, Adv. Mater. 31 (2019) 1805833.

[36] H. Liu, J. Li, L. Wang, Y. Tang, B.Y. Xia, Y. Chen, Trimetallic PtRhNi alloy nanoassemblies as highly active electrocatalyst for ethanol electrooxidation, Nano Res. 10 (2017) 3324–3332.

[37] S.-H. Han, H.-M. Liu, P. Chen, J.-X. Jiang, Y. Chen, Porous trimetallic PtRhCu cubic nanoboxes for ethanol electrooxidation, Adv. Energy Mater. 8 (2018) 1801326.

[38] K. Wang, H. Du, R. Sriphathoorat, P.K. Shen, Vertex-type engineering of Pt-Cu-Rh heterogeneous nanocages for highly efficient ethanol electrooxidation, Adv. Mater. 30 (2018) 1804074.

[39] Y. Shen, B. Gong, K. Xiao, L. Wang, In situ assembly of ultrathin PtRh nanowires to graphene nanosheets as highly efficient electrocatalysts for the oxidation of ethanol, ACS Appl. Mater. Interfaces 9 (2017) 3535–3543.

[40] J. Gonzalez-Cobos, S. Baranton, C. Coutanceau, A systematic in situ infrared study of the electrooxidation of C3 alcohols on carbon-supported Pt and Pt-Bi catalysts, J. Phys. Chem. C 120 (2016) 7155–7164.

[41] M.E.P. Markiewicz, S.H. Bergens, Second order dependence on the surface fraction of Pt in Pt-Ru-adatom of the oxidation of 2-PrOH in base, J. Phys. Chem. C 119 (2015) 27212–27219.

[42] X. Yu, L. Cheng, Y. Liu, A. Manthiram, A membraneless direct isopropanol fuel cell (DIPAFC) operated with a catalyst-selective principle, J. Phys. Chem. C 122 (2018) 13558–13563.

[43] S. Tominaka, H. Nishizeko, S. Ohta, T. Osaka, On-chip fuel cells for safe and high-power operation: investigation of alcohol fuel solutions, Energy Environ. Sci. 2 (2009) 849–852.

[44] H. Liu, J. Ye, C. Xu, S.P. Jiang, Y. Tong, Electro-oxidation of methanol, 1-propanol and 2-propanol on Pt and Pd in alkaline medium, J. Power Sources 177 (2008) 67–70.

[45] Y. Kang, F. Li, S. Li, P. Ji, J. Zeng, J. Jiang, Y. Chen, Unexpected catalytic activity of rhodium nanodendrites with nanosheet subunits for methanol electrooxidation in an alkaline medium, Nano Res. 9 (2016) 3893–3902.

[46] Y. Kang, Q. Xue, R. Jin, J. Jiang, J. Zeng, Y. Chen, Rhodium nanosheets-reduced graphene oxide hybrids: a highly active platinum-alternative electrocatalyst for the methanol oxidation reaction in alkaline media, ACS Sustain. Chem. Eng. 5 (2017) 10156–10162.

[47] J. Bai, X. Xiao, Y.-Y. Xue, J.-X. Jiang, J.-H. Zeng, X.-F. Li, Y. Chen, Bimetallic platinum-rhodium alloy nanodendrites as highly active electrocatalyst for the ethanol oxidation reaction, ACS Appl. Mater. Interfaces 10 (2018) 19755–19763.

[48] Y.-Q. Kang, Q. Xue, Y. Zhao, X.-F. Li, P.-J. Jin, Y. Chen, Selective etching induced synthesis of hollow Rh nanospheres electrocatalyst for alcohol oxidation reactions, Small 14 (2018) 210801239.

[49] B. Jiang, C. Li, O. Dag, H. Abe, T. Takei, T. Imai, M.S.A. Hossain, M.T. Islam, K. Wood, J. Henzie, Y. Yamauchi, Mesoporous metallic rhodium nanoparticles, Nat. Commun. 8 (2017) 15581.

[50] Y.-N. Zhai, Y. Li, J.-Y. Zhu, Y.-C. Jiang, S.-N. Li, Y. Chen, The electrocatalytic performance of carbon ball supported RhCo alloy nanocrystals for the methanol oxidation reaction in alkaline media, J. Power Sources 371 (2017) 129–135.

[51] C.-S. Kuo, C.-R. Kao, W.-J. Chen, M.-Y. Lu, D.A. Cullen, B.T. Sneed, Y.-C. Chuang, C.-C. Yu, C.-H. Kuo, Aqueous synthesis of concave Rh nanotetrahedra with defect-rich surfaces: insights into growth-, defect-, and plasmon-enhanced catalytic energy conversion, Chem. Mater. 30 (2018) 4448–4458.

[52] N. Fujiwara, Z. Siroma, T. Ioroi, K. Yasuda, Rapid evaluation of the electrooxidation of fuel compounds with a multiple-electrode setup for direct polymer electrolyte fuel cells, J. Power Sources 164 (2007) 457–463.

[53] S.-i. Yamazaki, M. Yao, N. Fujiwara, Z. Siroma, K. Yasuda, T. Ioroi, Electrocatalytic oxidation of alcohols by a carbon-supported Rh porphyrin, Chem. Commun. 48 (2012) 4353–4355.

[54] G. Kresse, J. Furthmüller, Efficient iterative schemes for ab initio total-energy calculations using a plane-wave basis set, Phys. Rev. B 54 (1996) 11169–11186.

[55] G. Kresse, J. Furthmüller, Efficiency of ab-initio total energy calculations for metals and semiconductors using a plane-wave basis set, Comput. Mater. Sci. 6 (1996) 15–50.

[56] G. Kresse, J. Hafner, Ab initio molecular dynamics for liquid metals, Phys. Rev. B 47 (1993) 558–561.

[57] P.E. Blöchl, Projector augmented-wave method, Phys. Rev. B 50 (1994) 17953–17979.

[58] G. Kresse, D. Joubert, From ultrasoft pseudopotentials to the projector augmented-wave method, Phys. Rev. B 59 (1999) 1758–1775.

[59] J.P. Perdew, J.A. Chevary, S.H. Vosko, K.A. Jackson, M.R. Pederson, D.J. Singh, C. Fiolhais, Atoms, molecules, solids, and surfaces: applications of the generalized gradient approximation for exchange and correlation, Phys. Rev. B 46 (1992)

[60] H.J. Monkhorst, J.D. Pack, Special points for Brillouin-zone integrations, Phys. Rev. B 13 (1976) 5188–5192.

[61] S. Grimme, J. Antony, S. Ehrlich, H. Krieg, A consistent and accurate ab initio parametrization of density functional dispersion correction (DFT-D) for the 94 elements H-Pu, J. Chem. Phys. 132 (2010) 19.

[62] W. Zhang, X. Zhang, L. Chen, J. Dai, Y. Ding, L. Ji, J. Zhao, M. Yan, F. Yang, C.-R. Chang, S. Guo, Single-walled carbon nanotube induced optimized electron polarization of rhodium nanocrystals to develop an interface catalyst for highly efficient electrocatalysis, ACS Catal. 8 (2018) 8092–8099.

[63] G. Kumar, E. Nikolla, S. Linic, J.W. Medlin, M.J. Janik, Multicomponent catalysts: limitations and prospects, ACS Catal. 8 (2018) 3202–3208.

[64] C.-Y. Su, H. Cheng, W. Li, Z.-Q. Liu, N. Li, Z. Hou, F.-Q. Bai, H.-X. Zhang, T.-Y. Ma, Atomic modulation of FeCo-nitrogen-carbon bifunctional oxygen electrodes for rechargeable and flexible all-solid-state zinc-air battery, Adv. Energy Mater. 7 (2017) 1602420.

[65] G. Fu, X. Yan, Y. Chen, L. Xu, D. Sun, J.-M. Lee, Y. Tang, Boosting bifunctional oxygen electrocatalysis with 3D graphene aerogel-supported Ni/MnO particles, Adv. Mater. 30 (2018) 1704609.

[66] C. Huang, T. Ouyang, Y. Zou, N. Li, Z.-Q. Liu, Ultrathin NiCo$_2$P$_x$ nanosheets strongly coupled with CNTs as efficient and robust electrocatalysts for overall water splitting, J. Mater. Chem. 6 (2018) 7420–7427.

[67] J.-Y. Zhang, H. Wang, Y. Tian, Y. Yan, Q. Xue, T. He, H. Liu, C. Wang, Y. Chen, B.Y. Xia, Anodic hydrazine oxidation assists energy-efficient hydrogen evolution over a bifunctional cobalt perselenide nanosheet electrode, Angew. Chem. Int. Ed. 130 (2018) 7775–7779.

[68] H. Duan, N. Yan, R. Yu, C.-R. Chang, G. Zhou, H.-S. Hu, H. Rong, Z. Niu, J. Mao, H. Asakura, T. Tanaka, P.J. Dyson, J. Li, Y. Li, Ultrathin rhodium nanosheets, Nat. Commun. 5 (2014) 3093.

[69] N. Zhang, Q. Shao, Y. Pi, J. Guo, X. Huang, Solvent-mediated shape tuning of well-defined rhodium nanocrystals for efficient electrochemical water splitting, Chem. Mater. 29 (2017) 5009–5015.

[70] P.-C. Chen, M. Liu, J.S. Du, B. Meckes, S. Wang, H. Lin, V.P. Dravid, C. Wolverton, C.A. Mirkin, Interface and heterostructure design in polyelemental nanoparticles, Science 363 (2019) 959–964.

[71] Z.-c. Zhang, B. Xu, X. Wang, Engineering nanointerfaces for nanocatalysis, Chem. Soc. Rev. 43 (2014) 7870–7886.

[72] J. Wan, W. Chen, C. Jia, L. Zheng, J. Dong, X. Zheng, Y. Wang, W. Yan, C. Chen, Q. Peng, D. Wang, Y. Li, Defect effects on TiO$_2$ nanosheets: stabilizing single atomic site Au and promoting catalytic properties, Adv. Mater. 30 (2018) 1705369.

[73] T. Ouyang, Y.-Q. Ye, C.-Y. Wu, K. Xiao, Z.-Q. Liu, Heterostructures composed of N-doped carbon nanotubes encapsulating cobalt and β-Mo$_2$C nanoparticles as bifunctional electrodes for water splitting, Angew. Chem. Int. Ed. 58 (2019) 4923–4928.

[74] L. An, Y. Li, M. Luo, J. Yin, Y.-Q. Zhao, C. Xu, F. Cheng, Y. Yang, P. Xi, S. Guo, Atomic-level coupled interfaces and lattice distortion on CuS/NiS$_2$ nanocrystals boost oxygen catalysis for flexible Zn-air batteries, Adv. Funct. Mater. 27 (2017) 1703779.

[75] Y. Yang, M. Luo, W. Zhang, Y. Sun, X. Chen, S. Guo, Metal surface and interface energy electrocatalysis: fundamentals, performance fngineering, and opportunities, Chemistry 4 (2018) 2054–2083.

[76] S. Moniri, T. Van Cleve, S. Linic, Pitfalls and best practices in measurements of the electrochemical surface area of platinum-based nanostructured electro-catalysts, J. Catal. 345 (2017) 1–10.

[77] S. Zhang, Y.Y. Shao, G.P. Yin, Y.H. Lin, Electrostatic self-assembly of a Pt-around-Au nanocomposite with high activity towards formic acid oxidation, Angew. Chem. Int. Ed. 49 (2010) 2211–2214.

[78] E.D. Wang, J.B. Xu, T.S. Zhao, Density functional theory studies of the structure sensitivity of ethanol oxidation on palladium surfaces, J. Phys. Chem. C 114 (2010) 10489–10497.

[79] Z. Luo, J. Lu, C. Flox, R. Nafria, A. Genç, J. Arbiol, J. Llorca, M. Ibáñez, J.R. Morante, A. Cabot, Pd$_2$Sn [010] nanorods as a highly active and stable ethanol oxidation catalyst, J. Mater. Chem. A 4 (2016) 16706–16713.

6671–6687.